

Demonstrating the Use of the Spherical Fourier Bessel Basis for Large Scale Clustering Systematics Discovery and Mitigation with eBOSS

Sean Bruton,^{1,*} James R. Cheshire IV,¹ Olivier Doré,^{1,2} Henry S. Grasshorn Gebhardt,^{1,2} and Robin Y. Wen¹

¹*California Institute of Technology, Pasadena, CA 91125, USA*

²*Jet Propulsion Laboratory, California Institute of Technology, Pasadena, CA 91109, USA*

The Spherical Fourier-Bessel (SFB) basis, in separating the angular and radial modes of the power spectrum, permits a targeted identification and mitigation of systematics in clustering surveys while retaining more cosmological signal than traditional bases. We demonstrate this principle on the eBOSS DR16 LRG and QSO samples, identifying modes which may be contaminated by systematics. Our initial inference on the LRG sample yields an f_{NL} value consistent with zero, while the QSO value is in slight tension with zero. Using the SFB basis, we vary the selection of angular and radial modes to search for inconsistencies in the inferred value of f_{NL} , an indicator of underlying systematics. In the QSO sample, we find evidence ($p < 0.005$ compared to the same cuts on EZMocks) of a systematic afflicting large physical scales, which is consistent with residual stellar contamination; we also find evidence ($p < 0.05$) for an unknown systematic in the QSO and LRG samples at the approximate angular plate and imaging scale of eBOSS.

Keywords: cosmology; large-scale structure

I. INTRODUCTION

Ongoing and imminent galaxy surveys, such as DESI (Adame *et al.* 2025), SPHEREx (Doré *et al.* 2014, Bock *et al.* 2026), Rubin/LSST (Ivezić *et al.* 2019), Euclid (Euclid Collaboration *et al.* 2025), and Roman (Eifler *et al.* 2021) are or will soon be measuring the 3-dimensional large-scale structure (LSS) of the Universe with unprecedented statistical precision. Advances in technology, infrastructure, and in observational and computational techniques mean that these surveys will measure $\mathcal{O}(10^9)$ galaxies over an unparalleled cosmological volume. With such advances in statistical precision, however, small subtleties in modeling or contamination from various sources of systematic error will dominate uncertainties and demand detailed understanding.

One key goal of the latest generation of galaxy surveys is to measure the deviation of the spectrum of primordial perturbations from that of a normal distribution; so-called “primordial non-Gaussianity”. Local-type non-Gaussianity, parameterized by $f_{\text{NL}}^{\text{loc}}$ (hereafter f_{NL}) (Komatsu and Spergel 2002, Dalal *et al.* 2008), will be particularly well-constrained with these datasets. The current leading constraint comes from the cosmic microwave background (CMB) bispectrum results from the Planck Collaboration (Planck Collaboration *et al.* 2020a), $f_{\text{NL}} = 0.9 \pm 5.1$. However, inherently 2-dimensional CMB observations are nearly limited by cosmic variance, suggesting 3-D surveys of large-scale structure as the natural avenues to furthering constraints on f_{NL} . A challenge is that accurate constraints on f_{NL} from large-scale structure require uncontaminated measurements of galaxy clustering on very large scales. These large scales are those which are particularly severely affected by var-

ious observational and instrumental systematic effects, necessitating careful characterization and mitigation.

Various approaches have been used to mitigate systematic effects in LSS surveys, with some analyses leveraging a combination of strategies. Full simulation of systematic effects and marginalizing over them in the inference step (e.g. Modi *et al.* (2019)) can be a powerful technique for systematic effects which are themselves well-modeled, but can be computationally expensive. Another common technique utilizes systematic template deprojection, where template maps are regressed against the observed galaxy density fields to correct for the modulation of the density field by the contaminant (Weaverdyck and Huterer 2021). Both of these approaches rely on understanding the landscape of and the modeling of individual systematic effects, thus different approaches must be used to identify and mitigate unknown or unmodeled systematic effects. Unknown systematics can be probed by injecting synthetic sources with known properties and propagating them through the analysis procedure, e.g. Everett *et al.* (2022). This can yield a measurement of the transfer function accounting for many systematics, though it is also computationally expensive, and relies on the accurate simulation of any instrumental effects. Yet another common technique, which will be the focus in this paper, is the explicit removal (or down-weighting) of specific scales/modes which are suspected of being systematically contaminated. These may often be identified through various data splits and consistency tests.

This latter “mode-cutting” approach is typically a powerful way of ensuring that the resulting dataset is uncontaminated, but may also remove significant amounts of cosmological signal. In Chaussidon *et al.* (2025), extensive template-based systematic regression is applied, however significant differences in the measured power spectrum are still found between different observing regions for the LRG sample after re-weighting to account for the effects captured by the templates, suggesting re-

* sbruton@caltech.edu

maining un-modeled systematic contamination at large scales. This was addressed by increasing the minimum wavenumber k_{\min} from 0.003 hMpc^{-1} to 0.006 hMpc^{-1} , though at the cost of a $\sim 30\%$ degradation in constraints on f_{NL} for the LRG sample alone. Unlike the cosmological signal, systematics, e.g. stars (Wen *et al.* 2025), are generally not homogeneous and isotropic. Due to their association with the observer position, systematics tend to be associated with a spherical geometry; however, typical power spectrum estimators are not naturally suited for the separation of angular and radial effects. Because of this, power spectrum estimators (e.g. Yamamoto *et al.* (2006)) entangle angular and radial information and any associated cuts (e.g., cuts on k_{\min}) remove both systematics and signal, when a more natural geometry allows one to cut systematics in an isolated way.

The Spherical Fourier-Bessel (SFB) formalism described in §II overcomes many of these deficiencies by matching the geometry of the estimator to the intrinsic geometry of realistic galaxy surveys: that of an observer situated at the center of a spherical geometry. By working in a spherical basis, wide-angle effects that arise from flat-sky approximations in Cartesian estimators are naturally captured, and effects related to observation rather than to cosmology (i.e., systematics) are more easily distinguished. The inherent 3-dimensional nature of the SFB basis, its large number of available modes, and its alignment with the geometry of observation make it a powerful framework with which to conduct cosmological analyses of large-scale structure, and particularly suit it to the mode-cutting approach to systematics mitigation. Systematics will be both more readily identified and less entangled with cosmology in this basis, meaning more precise cuts can be made with minimized loss of useful cosmological information. The effectiveness of mode cutting at mitigating systematics in the context of the SFB formalism was recently demonstrated in Wen *et al.* (2025).

The SuperFaB¹ SFB estimator was presented in Grasshorn Gebhardt and Doré (2021) and validated on a variety of simulations (including both “complete” and “realistic” EZmock simulations (Zhao *et al.* 2021)) in Grasshorn Gebhardt and Doré (2024). Using a covariance constructed from 1000 EZmock realizations, the SuperFaB estimator was able to obtain unbiased constraints on f_{NL} as measured from 100 realizations.

This paper builds upon the EZmock validation result by applying the SuperFaB estimator to the extended Baryon Oscillation Spectroscopic Survey (eBOSS) DR16 luminous red galaxy (LRG) and quasi-stellar object (QSO) samples (Ross *et al.* 2020) to produce constraints on f_{NL} , before proceeding to apply the results of Wen *et al.* (2025) in attempting to cut modes which are suspected to be contaminated. Previous efforts to

constrain f_{NL} using standard Fourier-space power spectrum multipole analyses applied to eBOSS QSOs include Castorina *et al.* (2019) (using the DR14 release), Qin *et al.* (2019), and Cagliari *et al.* (2024) (using the DR16 release). Cagliari *et al.* (2024) obtain a constraint $-4 < f_{\text{NL}} < 27$ at 68% confidence, though they themselves note a suspicion of residual systematic contamination based on the suboptimality of the constraint as compared to Fisher matrix-based forecasts. Cagliari *et al.* (2025) obtain a constraint $-6 < f_{\text{NL}} < 20$ at 68% confidence by using the Fourier-space bispectrum as well as the power spectrum to analyze the eBOSS DR16 QSO sample, noting that these results are consistent with expectations. The eBOSS LRG sample has been less used for f_{NL} analyses², while the BOSS DR12 galaxy sample, which mostly consists of LRGs, has been analyzed by both D’Amico *et al.* (2025) and Cabass *et al.* (2022) using the bispectrum in combination with the power spectrum.

For clarity, throughout this paper we define a “purely angular” systematic as one which solely *varies* angularly, i.e., where the modulation of the density field is purely a function of angle, $\Delta\delta(\mathbf{x}) \sim f(\hat{\mathbf{x}})$, where $f(\hat{\mathbf{x}})$ is some function of the normal vector $\hat{\mathbf{x}}$. Conversely, we define a “purely radial” systematic as one which solely *varies* radially, i.e., $\Delta\delta(\mathbf{x}) \sim Cf(x)$, where x denotes the magnitude of \mathbf{x} .

This paper is organized as follows: In §II, we review the spherical Fourier-Bessel formalism, and the modeling of relevant observational effects and of the galaxy-halo bias. In §III, we describe the eBOSS LRG and QSO datasets and present initial SFB-derived parameter constraints with the fiducial mode selection. In §IV, we describe the motivation, procedure and results of the systematic-cleaning mode-cutting when performed on the eBOSS LRG and QSO datasets and discuss the systematics possible physical origins. Finally, we conclude in §V.

In this work, all theoretical calculations and redshift-to-distance conversion assume a best-fit Planck 2018 Λ CDM cosmology (Planck Collaboration *et al.* 2020b).

II. SPHERICAL FOURIER-BESSEL FORMALISM

The SFB basis is composed of eigenfunctions of the Laplacian in spherical coordinates, namely the product of the angular basis functions, spherical harmonics $Y_{\ell m}^*(\hat{\mathbf{x}})$, and the radial basis functions $g_{n\ell}(x)$. The radial functions are the linear combinations of the spherical Bessel functions of the first kind and second kind (Samushia 2019):

$$g_{n\ell}(x) = c_{n\ell} j_{\ell}(k_{n\ell}x) + d_{n\ell} y_{\ell}(k_{n\ell}x), \quad (1)$$

¹ <https://github.com/hsgg/SphericalFourierBesselDecompositions.jl>

² The eBOSS LRG sample covers a smaller effective volume than the BOSS LRG sample due to its more limited sky area.

where $k_{n\ell}$ denotes the total Fourier magnitude (the eigenvalue of the Laplacian) of each SFB mode. The SFB modes are properly discretized under a spherical shell with finite comoving distance range $x_{\min} \leq x \leq x_{\max}$, with n denoting the index for wavenumber $k_{n\ell}$ at each angular multipole ℓ . The constants $c_{n\ell}$ and $d_{n\ell}$ are chosen to satisfy the orthonormality relation

$$\int_{x_{\min}}^{x_{\max}} dx x^2 g_{n\ell}(x) g_{n'\ell}(x) = \delta_{nn'}^K. \quad (2)$$

Beyond discretizing the SFB modes, the index n characterizes the number of zero-crossings in the radial basis functions, corresponding to the number of half-cycles in their radial oscillations (Wen *et al.* 2025). As such, increasing n captures finer structure along the radial direction. The separation between angular and radial scales is then achieved through the two indices ℓ and n in the SFB basis.

In this section, we describe the estimator and theory for SFB power spectrum. We emphasize that the formalism has been validated on eBOSS EZmocks (Grasshorn Gebhardt and Doré 2024), and it is sufficiently accurate for the statistical precision of eBOSS.

A. Estimator

We use the public code **SuperFaB** for estimating SFB power spectrum (PS). We refer the interested reader to Grasshorn Gebhardt and Doré (2021) and give only an overview here. For a galaxy catalog, the density fluctuation can be measured as

$$\delta^{\text{obs}}(\mathbf{x}) = w(\mathbf{x}) \frac{n_g(\mathbf{x}) - \alpha n_s(\mathbf{x})}{\bar{n}_{\max}}. \quad (3)$$

Here $n_g(\mathbf{x}) = W(\mathbf{x})n(\mathbf{x})$ is the observed galaxy number density under the window function $W(\mathbf{x})$, $n_s(\mathbf{x})$ is the number density for a synthetic random catalog, and α is the ratio of the number of observed galaxies in the catalog to the number of objects in the synthetic catalog. \bar{n}_{\max} is the maximum galaxy number density in the data catalog, and the window function is normalized to unity at the maximum number density in our convention.

We use the FKP weight $w(\mathbf{x})$ to improve the statistical power of power spectrum measurements (Feldman *et al.* 1994)

$$w(\mathbf{x}) = \frac{1}{1 + n_g(x) C_{\ell nn'}}, \quad (4)$$

where we approximate $C_{\ell nn'} \sim 3 \times 10^4 h^{-3} \text{Mpc}^3$ as a constant, and $n_g(x)$ is the observed radial number density of the galaxies. Optimal weights in SFB may take a different form than those proposed for the Cartesian Fourier-space power spectrum by Castorina *et al.* (2019), and we defer a study of this to future work.

The synthetic random catalog is generated such that it describes the expected density of observed galaxies under the survey geometry and selection in the absence of cosmological clustering

$$\alpha n_s(\mathbf{x}) = W(\mathbf{x})\bar{n}(x), \quad (5)$$

where $\bar{n}(x)$ is the estimated mean number density based on the data catalog

$$\bar{n}(x) = \frac{1}{\int d\hat{\mathbf{x}} W(\mathbf{x})} \int d\hat{\mathbf{x}} W(\mathbf{x}) n(\mathbf{x}). \quad (6)$$

Due to the difficulty of measuring radial selection function of galaxy surveys, we enforce the observed galaxy redshift distribution directly onto the synthetic random catalog (Eq. (5)). The effect of this procedure on the clustering statistics is known as the radial integral constraint (de Mattia and Ruhlmann-Kleider 2019), which we model in **II C**.

We can then perform the SFB transform as follows

$$\hat{\delta}_{n\ell m}^{\text{obs}} = \int d^3\mathbf{x} g_{n\ell}(x) Y_{\ell m}^*(\hat{\mathbf{x}}) \delta^{\text{obs}}(\mathbf{x}), \quad (7)$$

where the transform occurs over the spherical shell of $x_{\min} \leq x \leq x_{\max}$. We first perform the radial integral for each (n, ℓ) combination by directly summing over the galaxies (Leistedt *et al.* 2011) and pixelize on the spherical sky using the HEALPix scheme (Górski *et al.* 2005). The angular integration is then performed using HEALPix.jl (Tomas and Li 2021). This SFB transform is performed for both the data and the random catalogs.

Finally, we construct the pseudo-SFB power spectrum

$$\hat{C}_{\ell n n'}^{\text{obs}} = \frac{1}{2\ell + 1} \sum_m \hat{\delta}_{n\ell m}^{\text{obs}} \hat{\delta}_{n'\ell m}^{\text{obs}*}. \quad (8)$$

B. Power spectrum theory

Here we give an overview on the computation of the SFB power spectrum under the linear perturbation theory. We refer interested readers to Grasshorn Gebhardt and Doré (2021) and Wen *et al.* (2024) for theoretical and numerical details.

In the absence of window function, integral constraints, and shot noise, the theoretical SFB PS is

$$\langle \delta_{n\ell m} \delta_{n'\ell' m'} \rangle = \delta_{\ell\ell'}^K \delta_{mm'}^K C_{\ell nn'}. \quad (9)$$

The translational invariance is broken in the presence of redshift evolution and redshift space distortions (RSD), while the rotational invariance is still preserved. This leads to the angular mode ℓ and two radial modes n, n' (one for each argument of the two-point function) as a complete decomposition of the two-point statistics for the overdensity field.

Under linear Newtonian RSD, we can calculate the SFB power spectrum as (Grasshorn Gebhardt and Doré 2021)

$$C_{\ell n n'} = \int_0^\infty dq \mathcal{W}_{n\ell}(q) \mathcal{W}_{n'\ell}(q) P_{m,0}(q), \quad (10)$$

where $P_{m,0}(q)$ is the linear matter power spectrum at the present time, and q denotes the Fourier mode of the underlying matter field. The SFB kernel $\mathcal{W}_{n\ell}(q)$ is given by

$$\begin{aligned} \mathcal{W}_{n\ell}(q) = & \sqrt{\frac{2}{\pi}} q \int_{x_{\min}}^{x_{\max}} dx x^2 g_{n\ell}(x) D(x) \\ & \times e^{\frac{1}{2}\sigma_u^2 q^2 \partial_{qx}^2} [b(x, q) j_\ell(qx) - f(x) j_\ell''(qx)], \quad (11) \end{aligned}$$

where $g_{n\ell}(x)$ is the SFB radial basis functions defined in Eq. (1), D is the linear growth factor, and f is the linear growth rate.

The exponential operator in Eq. (11) describes the non-linear Gaussian velocity dispersion at small scales. We approximate the Gaussian damping by expanding the exponential operator (that acts on the spherical Bessels only) in a Taylor series to get (Grasshorn Gebhardt and Doré 2024)

$$e^{\frac{1}{2}\sigma_u^2 q^2 \partial_{qx}^2} j_\ell^{(d)}(qx) \approx j_\ell^{(d)}(qx) + \frac{q^2}{2} \sigma_u^2(x) j_\ell^{(d+2)}(qx),$$

where $j_\ell^{(d)}(qx)$ is the d th derivative with respect to qx . The velocity dispersion $\sigma_u(x)$ is a combination of the velocity dispersion for Fingers-of-God (FoG) effect and redshift measurement uncertainty.

Local non-Gaussianity is modeled via a scale-dependent bias (Dalal et al. 2008)

$$b(x, q) = b_1(x) + f_{\text{NL}} b_\phi(x) \frac{3\Omega_m H_0^2}{2q^2 T(q) \bar{D}(x)}, \quad (12)$$

where b_1 is the linear galaxy bias, and b_ϕ is the local PNG bias given the response to the presence of local PNG of the tracer. Here H_0 is the present Hubble parameter, $T(q)$ is the matter transfer function, and $\bar{D}(x)$ is the growth factor normalized to the scale factor a during matter domination $\bar{D}(x) = (1 + z_{\text{md}})^{-1} D(x)/D(x_{\text{md}})$, where the x_{md} indicates a time deep within matter domination.

The theoretical prescription of the local PNG bias b_ϕ has been under extensive discussion in recent literature³. Here we simply follow Slosar et al. (2008) and assume the following relation

$$b_\phi(x) = 2\delta_c(b_1(x) - p), \quad (13)$$

³ For recent examples, see Hadzhiyska and Ferraro (2025), Sullivan and Seljak (2025), Dalal and Percival (2025), Shivshankar et al. (2025), Perez et al. (2026), Moore et al. (2026) and the references therein.

where $\delta_c = 1.686$ is the critical density for spherical collapse and p quantifies the merger history of the tracer. Such forms of LPNG bias have been deployed in most PNG analyses to date. We use the universality relation ($p = 1$), that is assuming that their halo occupation distribution (HOD) depends only on halo mass (Tellarini et al. 2015), as the default for our analyses. This is consistent with the previous LRG analysis (Chaussidon et al. 2025). For the QSO sample, it is more customary in the literature to use $p = 1.6$ (Chaussidon et al. 2025, Castorina et al. 2019, Cagliari et al. 2024), assuming that all the quasars have a recent merger history (Slosar et al. 2008). We investigate the impacts of switching to $p = 1.6$ for our analyses in Section A 2.

To evaluate the SFB PS, the bulk of the computation is spent on the spherical Bessel functions in the SFB kernel $\mathcal{W}_{n\ell}(q)$ of Eq. (11). However, the Bessel functions only depend on the combination qx , not on q and x separately. Thus, we can choose discretizations for q and x such that in q - x space the “iso- qx ” lines go precisely through grid points. This Iso-qr integration method was proposed in Grasshorn Gebhardt and Doré (2024) and explained in detail in Wen et al. (2024), achieving evaluation of the SFB PS under linear Newtonian RSD on the order of seconds on a single CPU and enabling inference on data.

1. Chebyshev expansion

The linear galaxy bias b_1 is redshift-dependent for selected galaxy samples, and here we use the Chebyshev polynomials T_n up to the N^{th} order to model its redshift evolution

$$b_1(z) = \frac{\sum_{n=0}^N b_{1,n} T_n(\tilde{x}(z))}{D(z)}. \quad (14)$$

We performed the Chebyshev expansion over the normalized comoving distance $\tilde{x}(x(z)) = (x(z) - x_{\text{mid}})/\Delta x$ where $x_{\text{mid}} = \frac{1}{2}(x_{\text{max}} + x_{\text{min}})$ and $\Delta x = \frac{1}{2}(x_{\text{max}} - x_{\text{min}})$. The Chebyshev coefficients $b_{1,n}$ will be the fitting parameters. In practice, we find two coefficients provide a sufficient description for the bias evolution of both LRG and QSO samples, that is

$$b_1(z) = \frac{b_{1,0} + b_{1,1} \tilde{x}(z)}{D(z)}, \quad (15)$$

a linear function with respect to the comoving distance modulated by the growth factor. We tested using a quadratic function instead of the linear function and found that was not needed to emulate the bias’s redshift evolution. Figure 1 shows ten QSO EZmocks fit biases values against values from Cagliari et al. (2024), showing good agreement.

For the velocity dispersion including FoG and redshift errors, we also use Chebyshev polynomials to model the

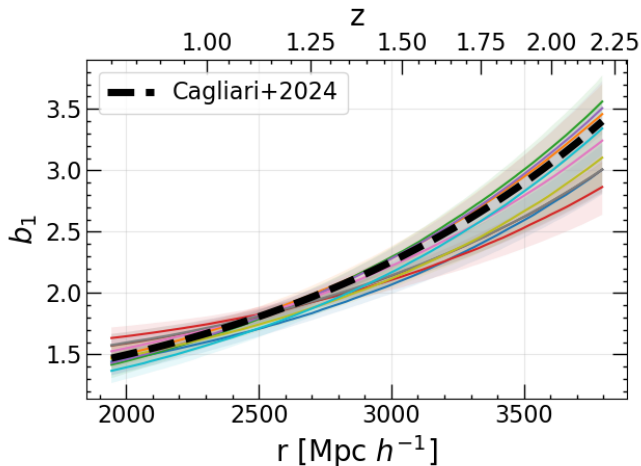


FIG. 1. The fit QSO bias for 10 EZMocks (colored lines, 16th and 84th quantiles shaded) as a function of radial distance. The upper axis shows the equivalent z . We overplot the fit from Cagliari *et al.* (2024) in black. There is good agreement between our EZMock fits and the result from Cagliari *et al.* (2024), validating our Chebyshev based bias model.

modulation over some fiducial velocity dispersions

$$\sigma_u(x) = \sigma_u^{\text{ref}}(x) \left(\sum_{n=0}^N \sigma_{u,n} T_n(\tilde{x}(x)) \right), \quad (16)$$

where the Chebyshev coefficients $\sigma_{u,n}$ allow marginalization over the dispersion uncertainties. For LRGs, we follow Grasshorn Gebhardt and Doré (2024) and use $\sigma_u^{\text{ref}}(x)^2 = f(x)^2 \sigma_{u,\text{fog}}^2 + \sigma_{u,z}^2$ that explicitly combines the FoG and redshift error components. The redshift measurement uncertainty is kept constant $1.05 h^{-1} \text{Mpc}$ across the LRG redshift range (Ross *et al.* 2020), while the FoG dispersion $\sigma_{u,\text{fog}}$ is set from the best fit to LRG EZmocks.

For the QSO sample we adopt a simpler modeling scheme with the fiducial function set to $\sigma_u^{\text{ref}} = 1$, letting the Chebyshev decomposition fully capture the redshift evolution. This is motivated by our experience with the LRG sample and explicit checks on the impacts of velocity dispersion, finding that the FoG evolution is simple enough to be captured by this model. In the default analysis, we fix LRG to its fiducial function, and set QSO only through the first Chebyshev coefficient with $\sigma_{u,0} = 5.5 h^{-1} \text{Mpc}$, obtained by fitting the QSO EZmocks, without marginalizing over the dispersion uncertainties. Due to the large redshift span and larger redshift uncertainties of QSO, we explicitly show the impact of marginalizing over the dispersion parameters for QSO inference in Section A 3, demonstrating that the dispersion modeling does not impact our results.

C. Estimator effects

In this work, we forward model the observational effects from the estimator, including window function, radial integral constraint, shot noise, and pixel windows, when compared to the SFB PS measurements. The ensemble average of the pseudo-SFB PS estimator (Eq. (8)) is related to the theoretical SFB PS (Eq. (10)) as the following

$$\begin{aligned} C_{\ell n_1 n_2}^{\text{obs}} &\equiv \langle \hat{C}_{\ell n_1 n_2}^{\text{obs}} \rangle \\ &= N_{\ell n_1 n_2}^{\text{obs}} + B_\ell \sum_{LN_1 N_2} \mathcal{A}_{\ell n_1 n_2}^{LN_1 N_2} C_{LN_1 N_2}, \end{aligned} \quad (17)$$

where $N_{\ell n_1 n_2}^{\text{obs}}$ is the shot noise, and B_ℓ is the angular HEALPIX pixel window function. There are no pixel window effects in the radial direction since the radial transform is done exactly without binning (Grasshorn Gebhardt and Doré 2021, Leistedt *et al.* 2012).

The PS mixing matrix \mathcal{A} depends on the window (including weight) matrix wW and the integral constraint matrix wG (Wen *et al.* 2026)

$$\mathcal{A} = \mathcal{M}[wW - wG, wW - wG]. \quad (18)$$

Here we use the notation $\mathcal{M}[A, B]$ to denote the azimuthally averaged contraction between two SFB matrices A and B

$$\mathcal{M}[A, B]_{\ell n_1 n_2}^{LN_1 N_2} = \frac{1}{2\ell + 1} \sum_{m, M} A_{n_1 \ell m}^{N_1 LM} B_{N_2 LM}^{n_2 \ell m}. \quad (19)$$

The window mixing matrix (including weight) in the SFB space is a double SFB transform of $w(\mathbf{x})W(\mathbf{x})$

$$\begin{aligned} (wW)_{n_\rho \ell_\rho m_\rho}^{n_\mu \ell_\mu m_\mu} &= \int d^3 \mathbf{x} g_{n_\rho \ell_\rho}(x) Y_{\ell_\rho m_\rho}^*(\hat{\mathbf{x}}) \\ &g_{n_\mu \ell_\mu}(x) Y_{\ell_\mu m_\mu}(\hat{\mathbf{x}}) w(\mathbf{x}) W(\mathbf{x}), \end{aligned} \quad (20)$$

and the mixing matrix for radial integral constraints are

$$(wG)_{n_\rho \ell_\rho m_\rho}^{n_\mu \ell_\mu m_\mu} = 4\pi \sum_{n'} (wW)_{n_\rho \ell_\rho m_\rho}^{n' 00} \tilde{W}_{n' 00}^{n_\mu \ell_\mu m_\mu}, \quad (21)$$

where \tilde{W} is the radially normalized window function $\tilde{W}(\mathbf{x}) = W(\mathbf{x}) / \int d\hat{\mathbf{x}} W(\mathbf{x})$. Our transform and index notations for the window functions and integral constraints exactly follow Sec. IV of Wen *et al.* (2026). We refer readers to Grasshorn Gebhardt and Doré (2024) and Wen *et al.* (2026) for the details on computing these mixing matrices from random catalogs. All above matrices arise from purely geometric effects for observations with no cosmological dependence.

III. INFERRING f_{NL} FROM LRGS AND QSOS

A. EBOSS

The data used herein are from the final extended Baryon Oscillation Spectroscopic Survey (eBOSS) catalogs, constructed from the Sloan Digital Sky Survey

(SDSS)-IV Data Release 16 (DR16), described in detail in [Ross et al. \(2020\)](#). The eBOSS DR16 LRG North Galactic Cap (NGC) sample contains 107,500 galaxies with spectroscopically measured redshifts over a range $0.6 < z < 1.0$ and an angular extent of $2,566 \text{ deg}^2$, representing the combination of the eBOSS LRG sample and the overlapping portion of the SDSS-III BOSS LRG sample ([Reid et al. 2016](#)). The NGC QSO sample contains 218,209 quasars over a redshift range $0.8 < z < 2.2$ and an area $2,924 \text{ deg}^2$. Data are also provided for the South Galactic Cap (SGC), though only those from the NGC are analyzed herein to avoid confounding systematics across the two fields, which may differ.

For each tracer and coverage region, random catalogs are provided alongside the galaxy catalogs at a $50\times$ higher density with randomly shuffled redshifts. Three distinct sets of completeness weights are provided: “close-pair” weights w_{cp} which correct for the density modulation by spectroscopic fiber collision; “no z ” weights w_{noz} which correct for the redshift failure rate; and imaging systematics weights w_{sys} which attempt to correct systematic density modulations inherited from the associated imaging survey. The total completeness weight is then taken as the product of these, $w_c = w_{\text{cp}} w_{\text{noz}} w_{\text{sys}}$.

The associated EZmock mock catalogs ([Zhao et al. 2021](#)) were constructed using the Effective Zel’dovich approximation and a standard flat Λ CDM cosmology with $\Omega_m = 0.31$. Both “complete” and “realistic” catalogs are provided, the former representing an ideal galaxy catalog observed perfectly, free from any observational effects, and the latter representing catalogs which have had all known observational and systematic effects applied to both the data and random catalogs.

B. Likelihood and Covariance Matrix

In this section, we briefly describe our procedure for constructing the likelihood and obtaining parameter constraints. More details are provided in [Grasshorn Gebhardt and Doré \(2024\)](#).

We use a Gaussian likelihood for the power spectrum,

$$\ln \mathcal{L} = \text{const} - \frac{1}{2} \Delta^T M^{-1} \Delta, \quad (22)$$

where Δ is the difference between the measured and theoretical SFB power spectra, and we estimate the covariance matrix M from the 1000 realistic EZmocks.

However, since the number of modes in the SFB power spectrum is a factor of a few larger than 1000, the covariance matrix obtained from these simulations has a large number of vanishing eigenvalues. In order to still use this estimate, we use the procedure described in [Wang et al. \(2020\)](#) to derive an optimal compression of the data vector based on the nonzero eigenvectors of the covariance matrix. In brief, we perform an eigendecomposition of the full covariance matrix, then we assemble a compression matrix R from the eigenvectors corresponding

to nonzero eigenvalues. Our data vector and covariance matrix then become

$$\Delta = R \cdot (\hat{C}_{\ell n n'}^{\text{obs}} - C_{\ell n n'}^{\text{theory}}), \quad (23)$$

$$M = R \cdot \hat{\Sigma} \cdot R^T, \quad (24)$$

where $\hat{\Sigma}$ is the full covariance matrix estimated from the 1,000 EZmocks. The compression matrix R projects the power spectrum onto the linear combination of modes that had a successful covariance estimate.

The likelihood in Eq. (22) is sampled by an Adaptive Metropolis-Hastings (AMH) sampler ([Roberts and Rosenthal 2009](#)), which we restart several times for faster convergence. The AMH sampler adjusts the proposal distribution every few steps by estimating a new proposal distribution from previous samples. Thus, it is Markovian asymptotically. We restart the sampler with an initial parameter vector nearer the maximum likelihood, and with a proposal distribution estimated from the previous run. This helps with achieving the asymptotic state of the AMH quicker.

The full set of parameters considered in the inference in the main text is $\{b_{1,0}, b_{1,1}, f_{\text{NL}}\}$, where $b_{1,i}$ parameterize the linear galaxy bias in Eq. (15). We always marginalize over the two linear bias parameters in inference. In Section A 3, we additionally marginalize over $\{\sigma_{u,i}\}$, which parametrize the velocity dispersion in Eq. (16).

C. Baseline f_{NL} Inference

With the eBOSS LRG and QSO datasets, SFB estimator, likelihood, and covariance in hand, we can perform inference on the set of parameters.

As an initial set of minimal cuts, we impose that ℓ_{min} is 8 – this removes the largest of the angular scales that exceeded the limited footprint of the survey. As can be seen by comparing the upper- and lower-left panels in Figure 4, removing the $\ell < 8$ modes cuts modes which are rapidly approaching zero due to the integral constraint. We impose that $0.0 < k < 0.08 \text{ h/Mpc}$ which excludes small scales where nonlinearity becomes non-negligible. Finally, we choose that $\Delta n < 2$, where $\Delta n = (n - n')$ which removes modes beyond the first two off-diagonals of $C_{\ell n n'}$; for $\Delta n > 2$, the power spectrum rapidly approaches zero.

[Grasshorn Gebhardt and Doré \(2024\)](#) showed that the estimator, in the ensemble, recovers an $f_{\text{NL}} = 0$ signal in mocks. We would like to extend this conclusion to our set of cuts. To do so, we make an initial inference on f_{NL} , $b_{1,0}$, and $b_{1,1}$ from 100 EZmocks to quantify any bias in the posterior of f_{NL} and quantify the expected scatter. Note that the compressed covariance (M , III B), which is used in the likelihood calculation for the AMH sampler, is recalculated after cutting the modes; in fact, the covariance is recalculated each time we make a unique set of mode cuts throughout the paper. The distribution of f_{NL} from the EZmocks is shown in Figure 2. We can see

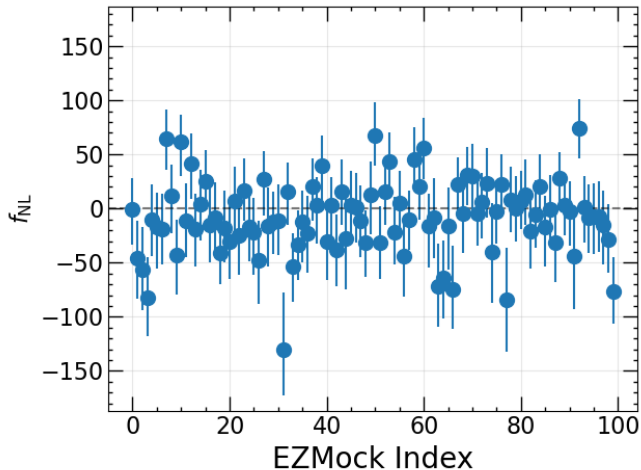


FIG. 2. The inferred median f_{NL} values for 100 LRG EZMocks with $\ell_{\text{min}} = 8$ when fitting for f_{NL} and the bias parameters. The error bars are the 16th and 84th quantile of the posterior. The median value across all 100 EZmocks is $f_{\text{NL}} = -8$ with $\frac{\sigma_{f_{\text{NL}}}}{\sqrt{N}} = 3.4$. The estimator is slightly negatively biased, but at a magnitude much smaller than the variances in f_{NL} that we will attempt to probe in this paper.

in Figure 2 that the inferred f_{NL} value is consistent with zero at about the expected rate. The median recovered f_{NL} value is -8 ± 3.4 , so the estimator is marginally negatively biased but at a magnitude that will prove to be insignificant for this paper.

We then make the same selections on the LRG and QSO data vectors and do the inference on f_{NL} , $b_{1,0}$, and $b_{1,1}$. Figure 3 shows the resulting corner plots from these inferences. The LRG posterior on f_{NL} has a median and 16th and 84th quantiles at $f_{\text{NL}} = -1^{+28}_{-31}$ (we will use the 16th and 84th quantiles as error bars on the posterior distribution of f_{NL} throughout the paper). This constraint is consistent with values derived from Planck (Planck Collaboration *et al.* 2020a) and LSS surveys (Castorina *et al.* 2019, Leistedt *et al.* 2014). The QSOs inferred f_{NL} value, however, is in slight tension with $f_{\text{NL}} \simeq 0$, with $f_{\text{NL}} = 38^{+25}_{-23}$.

IV. CONSISTENCY CHECKS

With the SFB basis we can push deeper into the inferred f_{NL} values. One may expect that systematics in the data may be (at least fairly) localized to particular angular or radial modes—for example, the characteristic angular size of the scan strategy of the survey or a redshift solution that gets particularly favored by the interference of a sky emission line that is not fully mitigated. We will now make a variety of cuts on SFB modes, rerun the inference, and check for self consistency on the inferred cosmological parameters, finding hints of residual systematics along the way.

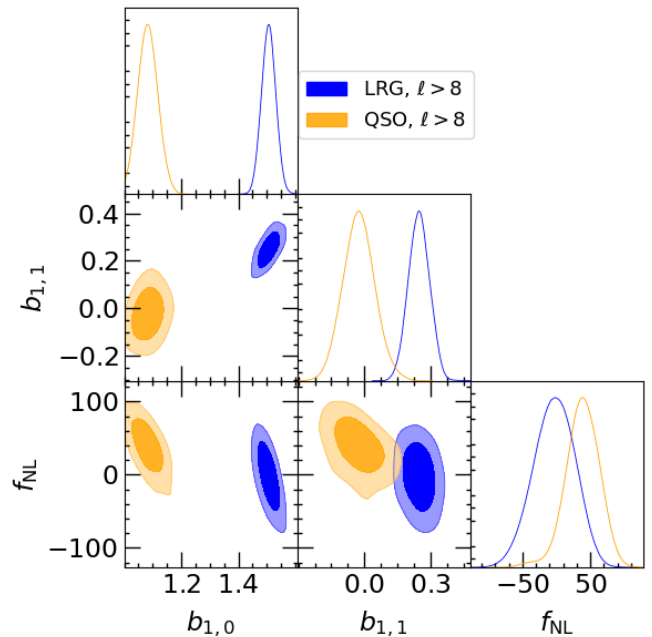


FIG. 3. The posterior distributions on the bias parameters and f_{NL} for the LRG and QSO samples with $\ell_{\text{min}} = 8$. The LRGs f_{NL} posterior is zero centered at $f_{\text{NL}} = -1^{+28}_{-31}$ while the QSOs f_{NL} posterior is in slight tension with zero at $f_{\text{NL}} = 38^{+25}_{-23}$.

The core idea behind our systematics identification procedure is that if one measures an SFB power spectrum data vector where all response is sourced by true cosmological signal, there should be consistency between the inferred values of f_{NL} when removing angular and/or radial modes to within the error bars at the expected rates from Gaussian statistics. Thus, the fundamental workflow for our systematic hunt exploits the consistency of inference (or lack thereof) when dropping modes and redoing the inference. If the data were free from systematics, dropping modes would decrease the constraining power on f_{NL} and the other fit parameters, but the new inferred value would be consistent with the old. This would manifest as inferred f_{NL} values fluctuating about the original value with increased error bars on the parameter, but the value would be consistent. If, on the other hand, there are systematics present in the data, dropping the modes afflicted by systematics may result in the inferred value of f_{NL} changing drastically, moving to a new value far outside the original error bars—further, the magnitude of the error bars themselves may change rapidly.

It is useful to look at plots of the SFB power spectrum for the EZMocks with some of the cuts that we will consider. Figure 4 shows the average of 1,000 measured QSO EZMocks' SFB power spectra in four panels: the full data vector in the top left, the $n=0$ mode only in the top right, the $\ell > 8$ modes in the bottom left, and only the on-diagonals ($n = n'$) in the bottom right. We will

explore the impact of making cuts of these types on the data vector to test how the inferred value of f_{NL} changes. Some key things to note and keep in mind:

1. A given n mode expresses as a continuous “trace” in the SFB power spectrum with ℓ increasing as effective k increases (the upper right panel shows the $n=0$ mode and its first two off-diagonals),
2. low ℓ modes tend to turn over and rapidly approach zero power across n modes (compare the modes removed between the upper- and lower-left panels), a result of the integral constraint, and
3. off diagonals ($n \neq n'$) tend to cluster near zero, a reflection of cosmological homogeneity (lower right panel) (Khek *et al.* 2024).

A. Radial Cuts

We take one LRG EZMock and successively increase the lowest n kept in the data vector, n_{min} and infer f_{NL} . Note that all of the cuts also include an $\ell_{\text{min}} = 8$ cut to remove modes which are too large to be probed by the survey footprint. Cutting the $n = 0$ modes (i.e. imposing $n_{\text{min}} = 1$) is equivalent to cutting power that varies only angularly, and is constant radially. Further, following the finding that stellar contamination tends to localize in the $n = 0$ and low ℓ modes (Wen *et al.* 2025), we set this n_{min} threshold only for $\ell < 20$; in Figure 5 we show the inferred f_{NL} value for the progressively increasing n_{min} where $\ell < 20$ for both the data and one EZMock. The error bars on each point are the 16th and 84th quantiles of the posterior on f_{NL} .

Note that Wen *et al.* (2025) find that the stellar contamination localizes to $n = 0$, $\ell \lesssim 50$, but the threshold value of ℓ depends on the redshift of the sample, the contamination rate, and the contamination mechanism. Our results do not significantly change if we change this ℓ threshold.

Figure 5 shows no strong features in the data—there is a gradual rise and fall in the inferred f_{NL} values in both the EZMock and LRGs that look to be consistent with each other. Thus, in this test we do not find evidence for systematics localized to the radial modes in the LRG sample.

We will now consider the same exercise but varying ℓ_{min} instead of n_{min} .

B. Angular Cuts

Similar to before, we take one LRG EZMock and successively increase the lowest ℓ kept in the data vector, ℓ_{min} (again starting with $\ell_{\text{min}} = 8$), and infer f_{NL} . We repeat the same exercise for the actual data measurements for the eBOSS LRG data. The results for both

are shown in Figure 6 with the EZMock in the left panel and the data in the right panel.

The EZMock, with input $f_{\text{NL}} = 0$, yields inferred f_{NL} values consistent with 0 and with no sharp features as a function of ℓ_{min} . The covariance of ℓ modes explains the gradual rise and fall of inferred f_{NL} , but the error bars on the points are consistent with zero at the expected rates.

The LRG data sample, on the other hand, displays sharp features where the inferred value of f_{NL} changes rapidly as we increase ℓ_{min} . The inference starts out at $f_{\text{NL}} \sim 0$ in the $8 \lesssim \ell_{\text{min}} \lesssim 24$ range, before rapidly decreasing to very negative $f_{\text{NL}} \sim -200$ values, and displaying more sporadic behavior at $\ell_{\text{min}} \gtrsim 60$. We can see that our initial inference, considered in Figure 3, may have actually serendipitously been centered about $f_{\text{NL}} \sim 0$ as a result of systematics canceling each other out. The sporadic behavior in inferred f_{NL} indicates that there are unaccounted for systematics in the sample and motivates cutting modes in the data vector to attempt to understand them better.

In Figures 5 and 6, we qualitatively looked for sharp features in the data that would indicate a systematic is present in either the angular or radial modes. Quantifying such features would be desirable but computationally expensive, and the physical interpretability of these Figures is challenging. A more fruitful allocation of resources is to use these Figures to motivate bin edges in a mode-binning scheme and do many inferences on EZMocks and the data using these binned modes. With the EZMocks, this permits the quantification of tension between the data vector’s inferred f_{NL} and the expected value for an $f_{\text{NL}} \sim 0$ universe. Binning modes is far more physically intuitive than the ℓ_{min} and n_{min} framework, since it allows us to identify parts of the data vector that appear to be afflicted by systematics, which can be directly mapped to angular scales. In this context, we investigate binning on the angular modes, with and without the $n = 0$ mode, to push for a deeper understanding.

C. Binned Angular Scales

For the binned angular scales analysis, we consider not just the LRGs, but also the eBOSS QSO sample. We consider each sample independently, making the same cuts on both samples and inferring f_{NL} from each sample separately.

Motivated by the results in Figures 5 and 6, we bin the ℓ modes for the LRG and QSO samples into ranges $8 \leq \ell \leq 32$, $33 \leq \ell \leq 64$, and $65 \leq \ell \leq 96$ and, to further investigate the impact of the $n = 0$ mode, we make these splits with and without the $n = 0$ mode included. We do the same splits across $N=50$ LRG and QSO EZMocks to quantify any discrepancies between the data and the EZMocks and to further stress test our modeling. The resulting inferred f_{NL} values for both the LRG and QSO samples are shown in Figure 7; the error bars on these points are the 16th and 84th quantiles from the

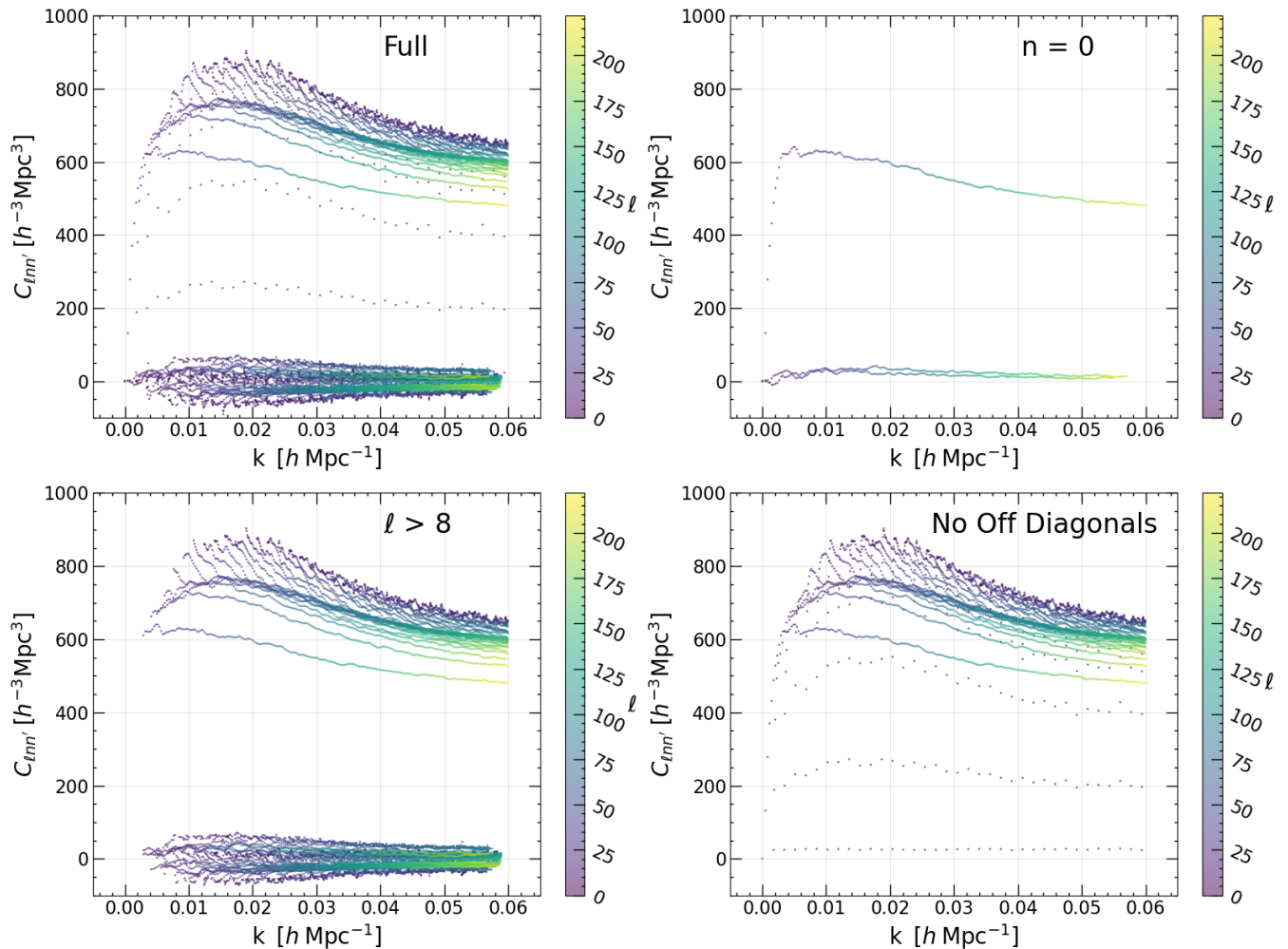


FIG. 4. Various cuts on the average measured SFB power spectrum for 1,000 QSO EZmocks. Top left: the entire SFB power spectrum. The ranges of n and ℓ considered can be determined by the chosen limits in k , in this case spanning $0 < n < 35$ and $0 < \ell < 222$. All points are color coded by ℓ for all plots on a set color scale. Top right: the $n = 0$ mode with two off-diagonals, $n' = 1$ and $n' = 2$. The two off-diagonals are at the bottom of the plot. Continuous traces in the full power spectrum correspond to fixed n . Bottom left: The SFB power spectrum with $\ell_{min} = 8$. The sharp downturns in the traces for all n are removed. Bottom right: Removing the off-diagonals, which are near zero. The remaining points near zero are the smallest ℓ modes for all n .

posteriors. We show the LRGs in the upper panels and the QSOs in the lower panels; the left panels include the $n = 0$ mode while the right panels excludes it. We fit the distribution of $N=50$ inferred f_{NL} values from the EZMocks for each scenario with a Gaussian and plot the mean inferred value (dashed line) and the 1-sigma deviations as colored bands, which allows us to calculate the p-values for the data with respect to the EZMock distribution of f_{NL} values. These p-values are reported in Table I and quantify the tension between the data and the EZMocks, which indicate that a systematic may be present in the modes considered.

There are many interesting features to digest in Figure 7 and Table I. First, including the $n = 0$ mode and considering the lowest ℓ range yields large positive f_{NL} values, with the QSO sample's value farther from zero

TABLE I. The p-values of the data with respect to the distribution defined by the EZMocks for a given set of cuts.

	$8 \leq \ell \leq 32$	$33 \leq \ell \leq 64$	$65 \leq \ell \leq 96$
LRG w/ $n = 0$	0.02	0.81	0.05
LRG w/out $n = 0$	0.22	0.88	0.06
QSO w/ $n = 0$	<0.005	0.88	0.01
QSO w/out $n = 0$	<0.005	1.00	<0.005

than the LRG sample; the p-value that the QSO data's f_{NL} value was drawn from the distribution defined by QSO EZMocks is very close to zero. When we remove the $n = 0$ mode, this tension is reduced owing almost entirely to a reduction in the offset from zero—the error bars stay approximately the same.

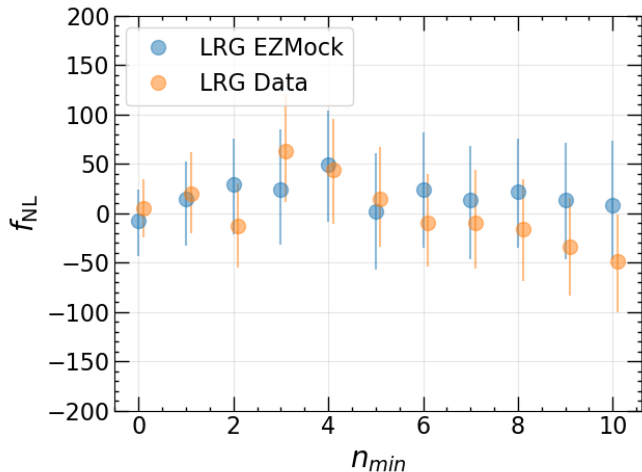


FIG. 5. Similar to Figure 6 but varying n_{min} . The evolution in n_{min} is qualitatively similar for the data and EZMock.

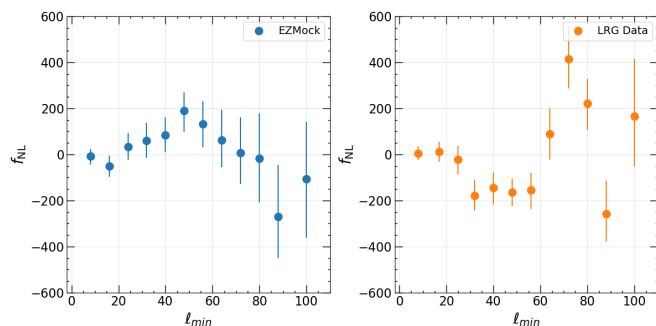


FIG. 6. Inferred f_{NL} as a function of ℓ_{min} for one randomly chosen EZmock (left panel) and the LRG sample (right panel). The covariance of ℓ modes is apparent in the EZmock plot, demonstrated in the correlated rise and fall with increasing ℓ_{min} . All but 5 of the points are consistent with $f_{NL} \sim 0$ (the input value for the EZmocks) to within their error bars, which increase in size as more modes are cut and less information is used. The LRG sample displays more sporadic behavior, starting out near zero before falling to extremely negative values that are significantly far from zero when accounting for the error bars. This is an indication that there are unmitigated systematics within the data vector, but does not help us localize them beyond a minimum ℓ .

There are thus two provocative pieces of information: 1) the low ℓ range is biased high and this bias is worse for the QSO sample and 2) removing the $n = 0$ mode from the QSO data vector removes a significant amount of this bias.

Recalling the [Wen et al. \(2025\)](#) result that stellar contamination largely resides in the ($n = 0$, $\ell \lesssim 50$) modes, one possible source of this systematic may be residual stellar contamination in the QSO sample. Foreground stars make identification of QSOs more difficult because of the increased background, which may imprint their clustering on to the QSO sample—the weights are meant

to mitigate this, but may not do a perfect job.

Another possibility comes from misidentification of QSOs and stars at the imaging level. The QSO target selection for eBOSS takes steps to remove stars from the proposed QSO sample—however, contamination at the imaging level is still expected, and although the contaminating stars will be nearly entirely removed from the QSO sample when their spectra are obtained, these stars may leave an imprint of stellar clustering on the QSO sample in two ways via fiber collisions.

Consider a true star and a true QSO near enough to each other to force a fiber collision, such that only one of these objects makes it into the QSO target sample. If the target preselection algorithm identifies both the star and the QSO as potential targets, the resulting fiber collision weight for whichever object is selected is increased. If the star is selected, targeted, identified to be a star, and discarded, we have missed a true QSO since there is no object in the QSO catalog to up-weight, as the star was rejected during the spectroscopy measurement. If the AGN is targeted, identified to be an AGN, and included in the sample, it is up-weighted to account for the fiber collision, though this weight was based on its collision with a star, not an AGN. Both of these failure modes imprint the stellar clustering onto the AGN clustering—the first through under-densities and the second through over-densities. In the auto power spectrum, both these under- and over-densities represent stellar-like clustering, which can contaminate large angular modes which are most sensitive to f_{NL} .

The middle ℓ bin gives an unbiased, though not particularly constraining inference on f_{NL} , a reflection of the fact that we have trimmed most of the modes and are not using a large data vector. However, its relative position compared to the blue and green points yields some insight about the features we saw in Figure 6, f_{NL} as a function of ℓ_{min} . In Figure 6, we saw that between $\ell_{min} = [8, 24]$, we inferred $f_{NL} \simeq 0$. However, Figure 7 shows that this was likely a serendipitous offsetting of different systematics that bias f_{NL} in opposite directions.

Finally, we consider the high ℓ bin. The LRG data points in both panels are biased towards very large negative f_{NL} albeit with a large error bar that is consistent with zero. The QSO data points, on the other hand, have approximately the same offset from zero in f_{NL} but with tighter error bars, putting them in strong contention with $f_{NL} \simeq 0$, the other ℓ bins, and the EZMocks; the p-values are both < 0.005 for the QSO inferred f_{NL} with respect to the EZMocks in this bin whether including the $n = 0$ mode or not. The consistency between the LRG and QSO values in all ℓ bins, particularly when removing the $n = 0$ mode, is both further validation of the estimator and evidence that the two samples share some unmitigated observer frame systematic, particularly in the lowest $8 \lesssim \ell \lesssim 32$. The QSOs appear to have a systematic affecting their $65 \lesssim \ell \lesssim 96$ bin which may be common with LRGs. It is noteworthy that this $65 < \ell < 96$ range roughly corresponds to the SDSS plate scale and the FoV

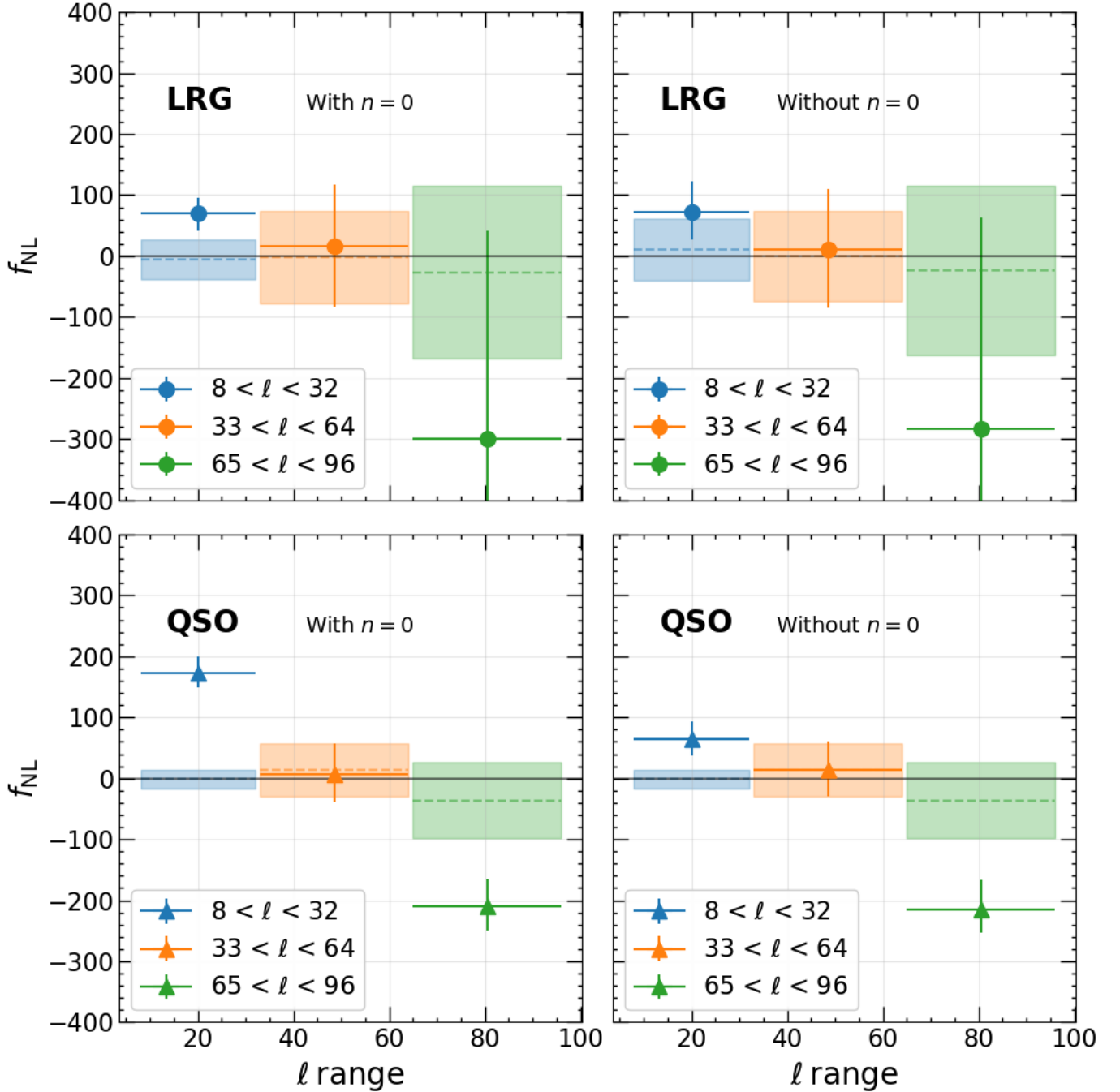


FIG. 7. Inferred f_{NL} for binned l ranges: $8 \leq l \leq 32$, $33 \leq l \leq 64$, and $65 \leq l \leq 96$ in blue, orange, and green, respectively, with LRGs in the upper panels and QSOs in the lower panels. Left panels are with the $n = 0$ mode and right panels are without it. The error bars are the 16th and 84th quantile from the posterior sampling. The horizontal dashed lines and shaded regions represent the mean and 1-sigma deviation of inferred f_{NL} from a population of 50 EZmocks with the same cuts. The QSOs' smallest l range, the blue point, shows signs of being afflicted by stellar clustering, which tends to impact the $n = 0$ and low l modes most strongly. Cutting the $n = 0$ mode brings it into agreement with LRGs (though still in tension with the EZMocks). The largest l bin, in green, shows a very strong negative bias for both samples, albeit with a large error bars for LRGs. This bin notably corresponds to the plate and imaging scale for eBOSS and its parent imaging survey.

of its parent imaging survey. In the course of attempting to isolate this systematic’s source, we cut the off-diagonals ($n \neq n'$), where inhomogeneity would localize in the SFB power spectrum, and found no improvement in the inferred f_{NL} value. We also tested against model misspecification, changing $p = 1.0$ to $p = 1.6$ and allowing more redshift evolution in our FoG modeling. Both of these, however, also failed to explain the strong negative f_{NL} bias. These adjustments and results are discussed in Appendix A. Proper diagnosis of this systematic beyond the investigations in the appendix would require efforts beyond the scope of this work, so we leave a deeper investigation to future researchers.

V. CONCLUSION

In this work, we analyzed the clustering of the eBOSS LRG and QSO samples in the SFB framework. We sought to demonstrate finer mode cutting and systematic isolation in the SFB basis. The SFB basis allows one to naturally decompose systematics into angular and radial components on the sky, reflecting the natural geometry of astrometric surveys.

We operate under the assumption that the eBOSS LRG and QSO samples, if free of systematics, would lead to an inference of $f_{\text{NL}} \sim 0$ to within error bars, consistent with previous CMB and the latest LSS measurements. In this way, we are taking a decidedly *unblinded* approach, using the inferred values of f_{NL} to search for problematic regions of the data vector which may be afflicted by systematics.

An initial inference of f_{NL} from the LRG and QSOs samples yields values of $f_{\text{NL}} = -1_{-28}^{+31}$ and $f_{\text{NL}} = 38_{-23}^{+25}$, a perfectly reasonable inferred value from the LRGs and only a slight tension with expectations from QSOs. We use the SFB basis to dig deeper, searching for inconsistencies in the inferred value of f_{NL} when we make particular mode cuts on the power spectrum, which would be an indicator of underlying systematics. We find that the $n = 0$ and $\ell < 20$ modes, i.e. large-scale angular only modes, in the QSOs seem to be impacted by a systematic; under the assumption that the inferred f_{NL} value is drawn from the same distribution as those from EZMocks with the same cuts applied, we calculate a p-value of < 0.005 . We

conjecture that the systematic could be associated with stellar contamination, either through weights which do not fully mitigate their impact or the result of the stellar population imprinting onto the QSO target sample at the imaging level stage.

We also find that the QSO and LRGs samples have evidence ($p < 0.05$) of a systematic in the $65 < \ell < 96$ range, which roughly corresponds to the plate and imaging scales for eBOSS and its parent imaging survey. We attempt to isolate and cut this systematic in the off-diagonals, where radial inhomogeneities would arise, but do not see the inferred f_{NL} value move towards zero after the cut. We rule out that the p value or FoG modeling are causing this tension.

The analysis in this paper, while a proof of concept in using SFB for systematic identification, could not be replicated in an analysis where one is trying to infer f_{NL} at a competitive level, where one cannot assume that $f_{\text{NL}} \sim 0$ at the level of the survey’s sensitivity. Instead, the best practice would be to adopt a blinded approach. In a future blinded analysis, the hunt for unknown systematics could be accomplished by dropping random subsets of modes, checking for consistency in f_{NL} , and isolating modes which are common in the failing consistency checks.

ACKNOWLEDGMENTS

The authors thank Alex Krolewski and Richard Feder for useful conversations that improved the paper’s discussion of possible stellar contamination in the QSO sample and for giving feedback on a draft of this manuscript. The authors also thank Héctor Gil-Marín for useful discussion. ©2026. All rights reserved. Part of this work was done at Jet Propulsion Laboratory, California Institute of Technology, under a contract with the National Aeronautics and Space Administration. RYW acknowledges support through the Canada Graduate Research Scholarship– Doctoral program (CGRS D) from the Natural Sciences and Engineering Research Council of Canada (NSERC). We acknowledge support from the SPHEREx project under a contract from the NASA/GODDARD Space Flight Center to the California Institute of Technology.

A. G. Adame, J. Aguilar, S. Ahlen, S. Alam, D. M. Alexander, M. Alvarez, O. Alves, A. Anand, U. Andrade, E. Armengaud, *et al.*, *J. Cosmology Astropart. Phys.* **2025**, 017 (2025), [arXiv:2411.12020 \[astro-ph.CO\]](#).

O. Doré, J. Bock, M. Ashby, P. Capak, A. Cooray, R. de Putter, T. Eifler, N. Flagey, Y. Gong, S. Habib, *et al.*, [arXiv e-prints](#), [arXiv:1412.4872 \(2014\)](#), [arXiv:1412.4872 \[astro-ph.CO\]](#).

J. J. Bock, A. M. Aboobaker, J. Adamo, R. Akeson, J. M. Alred, F. Alibay, M. L. N. Ashby, Y. P. Bach, L. E. Bleem, D. Bolton, *et al.*, *ApJ* **999**, 139 (2026), [arXiv:2511.02985 \[astro-ph.IM\]](#).

Ž. Ivezić, S. M. Kahn, J. A. Tyson, B. Abel, E. Acosta, R. Allsman, D. Alonso, Y. AlSayyad, S. F. Anderson, J. Andrew, *et al.*, *ApJ* **873**, 111 (2019), [arXiv:0805.2366 \[astro-ph\]](#).

Euclid Collaboration, Y. Mellier, Abdurro’uf, J. A. Acevedo Barroso, A. Achúcarro, J. Adamek, R. Adam, G. E. Addi-

- son, N. Aghanim, M. Aguena, *et al.*, *A&A* **697**, A1 (2025), [arXiv:2405.13491 \[astro-ph.CO\]](#).
- T. Eifler, H. Miyatake, E. Krause, C. Heinrich, V. Miranda, C. Hirata, J. Xu, S. Hemmati, M. Simet, P. Capak, *et al.*, *MNRAS* **507**, 1746 (2021), [arXiv:2004.05271 \[astro-ph.CO\]](#).
- E. Komatsu and D. N. Spergel, in *The Ninth Marcel Grossmann Meeting*, edited by V. G. Gurzadyan, R. T. Jantzen, and R. Ruffini (2002) pp. 2009–2010, [arXiv:astro-ph/0012197 \[astro-ph\]](#).
- N. Dalal, O. Doré, D. Huterer, and A. Shirokov, *Phys. Rev. D* **77**, 123514 (2008), [arXiv:0710.4560 \[astro-ph\]](#).
- Planck Collaboration, Y. Akrami, F. Arroja, M. Ashdown, J. Aumont, C. Baccigalupi, M. Ballardini, A. J. Banday, R. B. Barreiro, N. Bartolo, *et al.*, *A&A* **641**, A9 (2020a), [arXiv:1905.05697 \[astro-ph.CO\]](#).
- C. Modi, M. White, A. Slosar, and E. Castorina, *J. Cosmology Astropart. Phys.* **2019**, 023 (2019), [arXiv:1907.02330 \[astro-ph.CO\]](#).
- N. Weaverdyck and D. Huterer, *MNRAS* **503**, 5061 (2021), [arXiv:2007.14499 \[astro-ph.CO\]](#).
- S. Everett, B. Yanny, N. Kuropatkin, E. M. Huff, Y. Zhang, J. Myles, A. Masegian, J. Elvin-Poole, S. Allam, G. M. Bernstein, *et al.*, *ApJS* **258**, 15 (2022), [arXiv:2012.12825 \[astro-ph.CO\]](#).
- E. Chaussidon, C. Yèche, A. de Mattia, C. Payerne, P. McDonald, A. J. Ross, S. Ahlen, D. Bianchi, D. Brooks, E. Burtin, *et al.*, *J. Cosmology Astropart. Phys.* **2025**, 029 (2025), [arXiv:2411.17623 \[astro-ph.CO\]](#).
- R. Y. Wen, H. S. G. Gebhardt, C. Heinrich, and O. Doré, *Phys. Rev. D* **112**, 063518 (2025), [arXiv:2506.06902 \[astro-ph.CO\]](#).
- K. Yamamoto, M. Nakamichi, A. Kamino, B. A. Bassett, and H. Nishioka, *PASJ* **58**, 93 (2006), [arXiv:astro-ph/0505115 \[astro-ph\]](#).
- H. S. Grasshorn Gebhardt and O. Doré, *Phys. Rev. D* **104**, 123548 (2021), [arXiv:2102.10079 \[astro-ph.CO\]](#).
- C. Zhao, C.-H. Chuang, J. Bautista, A. de Mattia, A. Raichoor, A. J. Ross, J. Hou, R. Neveux, C. Tao, E. Burtin, *et al.*, *MNRAS* **503**, 1149 (2021), [arXiv:2007.08997 \[astro-ph.CO\]](#).
- H. S. Grasshorn Gebhardt and O. Doré, *Phys. Rev. D* **109**, 083502 (2024), [arXiv:2310.17677 \[astro-ph.IM\]](#).
- A. J. Ross, J. Bautista, R. Tojeiro, S. Alam, S. Bailey, E. Burtin, J. Comparat, K. S. Dawson, A. de Mattia, H. du Mas des Bourboux, *et al.*, *MNRAS* **498**, 2354 (2020), [arXiv:2007.09000 \[astro-ph.CO\]](#).
- E. Castorina, N. Hand, U. Seljak, F. Beutler, C.-H. Chuang, C. Zhao, H. Gil-Marín, W. J. Percival, A. J. Ross, P. D. Choi, *et al.*, *J. Cosmology Astropart. Phys.* **2019**, 010 (2019), [arXiv:1904.08859 \[astro-ph.CO\]](#).
- F. Qin, C. Howlett, and L. Staveley-Smith, *MNRAS* **487**, 5235 (2019), [arXiv:1906.02874 \[astro-ph.CO\]](#).
- M. S. Cagliari, E. Castorina, M. Bonici, and D. Bianchi, *J. Cosmology Astropart. Phys.* **2024**, 036 (2024), [arXiv:2309.15814 \[astro-ph.CO\]](#).
- M. S. Cagliari, M. Barberi-Squarotti, K. Pardede, E. Castorina, and G. D’Amico, *J. Cosmology Astropart. Phys.* **2025**, 043 (2025), [arXiv:2502.14758 \[astro-ph.CO\]](#).
- G. D’Amico, M. Lewandowski, L. Senatore, and P. Zhang, *Phys. Rev. D* **111**, 063514 (2025), [arXiv:2201.11518 \[astro-ph.CO\]](#).
- G. Cabass, M. M. Ivanov, O. H. E. Philcox, M. Simonović, and M. Zaldarriaga, *Phys. Rev. D* **106**, 043506 (2022), [arXiv:2204.01781 \[astro-ph.CO\]](#).
- Planck Collaboration, N. Aghanim, Y. Akrami, M. Ashdown, J. Aumont, C. Baccigalupi, M. Ballardini, A. J. Banday, R. B. Barreiro, N. Bartolo, *et al.*, *A&A* **641**, A6 (2020b), [arXiv:1807.06209 \[astro-ph.CO\]](#).
- L. Samushia, *arXiv e-prints*, [arXiv:1906.05866 \(2019\)](#), [arXiv:1906.05866 \[astro-ph.CO\]](#).
- H. A. Feldman, N. Kaiser, and J. A. Peacock, *ApJ* **426**, 23 (1994), [arXiv:astro-ph/9304022 \[astro-ph\]](#).
- A. de Mattia and V. Ruhlmann-Kleider, *J. Cosmology Astropart. Phys.* **2019**, 036 (2019), [arXiv:1904.08851 \[astro-ph.CO\]](#).
- B. Leistedt, A. Rassat, A. Refregier, and J. L. Starck, 3DEX: Fast Fourier-Bessel Decomposition of Spherical 3D Surveys, Astrophysics Source Code Library, record ascl:1111.011 (2011).
- K. M. Górski, E. Hivon, A. J. Banday, B. D. Wandelt, F. K. Hansen, M. Reinecke, and M. Bartelmann, *ApJ* **622**, 759 (2005), [arXiv:astro-ph/0409513 \[astro-ph\]](#).
- M. Tomasi and Z. Li, Healpix.jl: Julia-only port of the HEALPix library, Astrophysics Source Code Library, record ascl:2109.028 (2021).
- R. Y. Wen, H. S. G. Gebhardt, C. Heinrich, and O. Doré, *Phys. Rev. D* **110**, 123501 (2024), [arXiv:2407.02753 \[astro-ph.CO\]](#).
- B. Hadzhiyska and S. Ferraro, *Phys. Rev. D* **111**, 103521 (2025), [arXiv:2501.14873 \[astro-ph.CO\]](#).
- J. M. Sullivan and U. Seljak, *Phys. Rev. D* **112**, 083522 (2025), [arXiv:2503.21736 \[astro-ph.CO\]](#).
- N. Dalal and W. J. Percival, *arXiv e-prints*, [arXiv:2503.21024 \(2025\)](#), [arXiv:2503.21024 \[astro-ph.CO\]](#).
- C. Shiveshwarkar, M. Loverde, C. M. Hirata, and D. Jamieson, *arXiv e-prints*, [arXiv:2508.11798 \(2025\)](#), [arXiv:2508.11798 \[astro-ph.CO\]](#).
- L. A. Perez, S. Genel, E. Krause, and R. S. Somerville, *arXiv e-prints*, [arXiv:2602.04987 \(2026\)](#), [arXiv:2602.04987 \[astro-ph.CO\]](#).
- A. Moore, L. A. Perez, and E. Krause, *arXiv e-prints*, [arXiv:2604.21790 \(2026\)](#), [arXiv:2604.21790 \[astro-ph.CO\]](#).
- A. Slosar, C. Hirata, U. Seljak, S. Ho, and N. Padmanabhan, *J. Cosmology Astropart. Phys.* **2008**, 031 (2008), [arXiv:0805.3580 \[astro-ph\]](#).
- M. Tellarini, A. J. Ross, G. Tasinato, and D. Wands, *J. Cosmology Astropart. Phys.* **2015**, 004 (2015), [arXiv:1504.00324 \[astro-ph.CO\]](#).
- B. Leistedt, A. Rassat, A. Réfrégier, and J. L. Starck, *A&A* **540**, A60 (2012), [arXiv:1111.3591 \[astro-ph.CO\]](#).
- R. Y. Wen, H. S. Grasshorn Gebhardt, C. Heinrich, and O. Doré, *arXiv e-prints*, [arXiv:2601.19438 \(2026\)](#), [arXiv:2601.19438 \[astro-ph.CO\]](#).

B. Reid, S. Ho, N. Padmanabhan, W. J. Percival, J. Tinker, R. Tojeiro, M. White, D. J. Eisenstein, C. Maraston, A. J. Ross, *et al.*, *MNRAS* **455**, 1553 (2016), [arXiv:1509.06529 \[astro-ph.CO\]](#).

M. S. Wang, S. Avila, D. Bianchi, R. Crittenden, and W. J. Percival, *J. Cosmology Astropart. Phys.* **2020**, 022 (2020), [arXiv:2007.14962 \[astro-ph.CO\]](#).

G. O. Roberts and J. S. Rosenthal, *Journal of Computational and Graphical Statistics* **18**, 349 (2009), <https://doi.org/10.1198/jcgs.2009.06134>.

B. Leistedt, H. V. Peiris, and N. Roth, *Phys. Rev. Lett.* **113**, 221301 (2014), [arXiv:1405.4315 \[astro-ph.CO\]](#).

B. Khek, H. G. Gebhardt, and O. Doré, *Phys. Rev. D* **110**, 063524 (2024), [arXiv:2212.05760 \[astro-ph.CO\]](#).

Appendix A: Testing Against Model Misspecification

In this appendix, we review our attempts to isolate and explain the systematic which seems to be present in the QSO sample’s highest ℓ bin, $65 < \ell < 96$. Among the tests we considered were:

1. cutting the off-diagonals from the data vector,
2. changing the assumed p value, and
3. allowing a more flexible FoG model and fitting its parameters.

1. Off-Diagonals

Unaccounted for radial inhomogeneities in the data would manifest as excess power in the off-diagonals of the SFB power spectrum. Such radial inhomogeneities, on the largest scales, could arise from , e.g., systematics or FoG model misspecification. As such, it is reasonable to try cutting the off-diagonals, which may be where problematic systematics disproportionately contribute power, and see how the posteriors change.

Figure 8 shows the derived posteriors on f_{NL} for the LRG and QSO samples with and without the off diagonals included.

We see that, when removing the off-diagonals ($\Delta n = 0$), the quasar’s lowest ℓ bin comes into agreement with the LRG data points, indicating that the systematic in this bin, which we hypothesized in Section IV C was stellar contamination, is specifically contaminating the off-diagonal modes of the SFB power spectrum.

Further, the middle ℓ bin, when removing the off-diagonals ($\Delta n = 0$), shifts downward for both LRGs (though with an error bar consistent with zero) and QSOs by approximately the same amount. This may be an indication of systematics in the on- and off-diagonals that are canceling each other out, akin to the discussion in Section IV C.

Finally, the highest ℓ bin data points do not shift in a statistically significant way when removing the off-diagonals, indicating that the systematic does not reside in these modes.

2. Changing the value of p

The value of p , which, as described in Section II B, characterizes the merger history of the tracer, controls the response of a tracer to f_{NL} through b_ϕ , which is in turn fully degenerate with the value of f_{NL} . QSOs, in previous studies, are typically prescribed a value of $p = 1.6$, a divergence from the universality relation, reflecting that quasars, as a population average, have a recent merger. We test here the response of our inferred f_{NL} to the choice in the value of p .

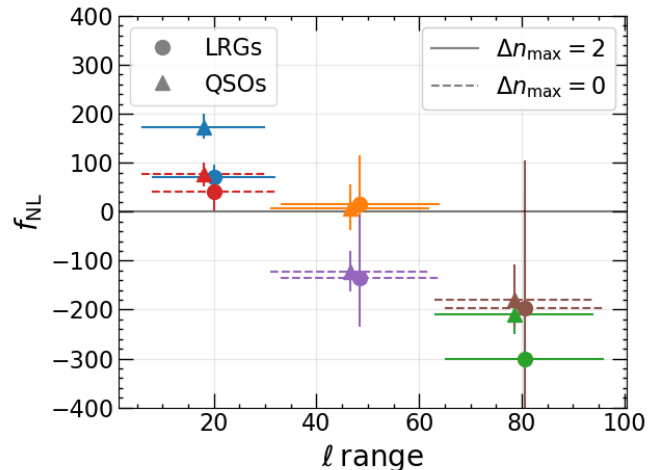


FIG. 8. Inferred values of f_{NL} with and without the off-diagonals for the same ℓ bins considered in Figure 7. When cutting the off-diagonals in the first ℓ bin, we gain the same benefits that we saw when cutting the $n = 0$ mode: the QSO population comes into agreement with the LRG sample. This indicates that the systematic, which we hypothesize is stellar contamination, is isolated to not just the $n = 0$ mode, but specifically the off-diagonal of the $n = 0$ mode. Cutting the off-diagonals does not alleviate the QSOs largest ℓ bin’s contention with zero (brown point) and creates a tension in the middle ℓ bin with zero, perhaps an indication of offsetting systematics in the middle ℓ bin in the on- and off-diagonals.

We begin by simply changing the value of p to 1.6 and redo the MCMC fitting for f_{NL} and the bias parameters for both the LRGs and QSOs. The LRG p value is not expected to be 1.6, but we vary it to test the dependence in the inferred value of f_{NL} on p . We show in Figure 9 the inferred f_{NL} values for both populations. Focusing first on the LRG population, we do not see variation in the inferred value of f_{NL} beyond the error bars when changing the value of p . Not so for the QSOs. In the lowest ℓ range bin, we see that our inferred value of f_{NL} is shifted by about 500, from 200 to -300 and both points have very tight error bars. The middle ℓ range is consistent and the largest ℓ range has a very slight tension, but nothing close to the lowest ℓ bin.

We determined that this behavior is a complex interplay between the value chosen for p , the fit bias parameters, and the systematic that is afflicting this bin. The bias relation for the $8 < \ell < 32$ bin for both $p = 1.0$ and $p = 1.6$ evolves in the opposite direction of the rest of the bins, going from high bias values to low bias values as z increases. In Figure 10, we show the fitting results when we vary the value of p and fit for the QSO bias versus fixing it at fiducial values to recreate the results from Cagliari *et al.* (2024). The lowest ℓ bin suddenly comes into agreement with $f_{\text{NL}} \sim 0$ when the bias is set instead of fit, indicating that the bias is not being fit well in this sample. Our hypothesis is that the stellar contamination afflicting this bin is rendering the fit bias

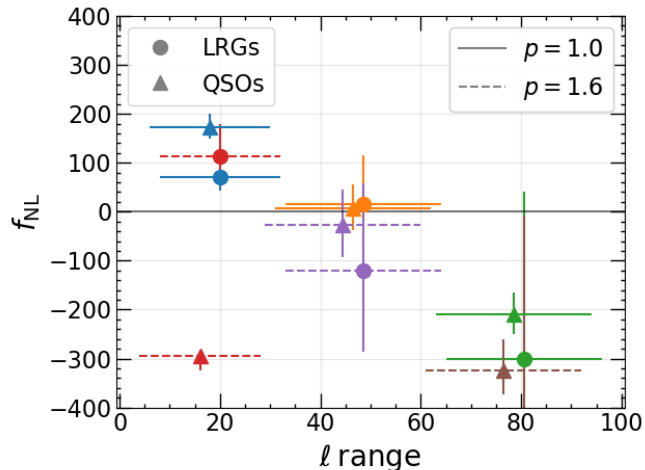


FIG. 9. Inferred values of f_{NL} when changing the value of p , which, in part, parameterizes the response of a sample to f_{NL} . The LRG sample is unaffected to within error bars in all ℓ bins. The QSOs lowest ℓ bin's inferred f_{NL} depends strongly on the chosen value of p , but, as discussed in the text and further explored in Figure 10, we believe this is due to an ill behaved bias fit, likely resulting from stellar contamination. The QSOs largest ℓ bin does not move towards zero significantly. The chosen value of p certainly matters, but the effect is not large enough to explain the largest ℓ bin's discrepancy with $f_{\text{NL}} \sim 0$.

values unphysical and that the inferred value of f_{NL} can then evolve very quickly, depending on the choice of p , because the bias values cross the value of 1.6. As one can see in Eqs. 12 and 13, when b_1 cross the value of p , the physical response of clustering of the tracers to f_{NL} changes sign.

While this makes interpretation of the lowest ℓ bin more challenging, it does not help explain the systematic in the $65 < \ell < 96$ bin. In fact, it made the discrepancy with $f_{\text{NL}} \sim 0$ more severe.

3. FoG Modeling

Finally, we consider that the FoG model has insufficient complexity to describe the real behavior, which we hypothesize could lead to a bias in the inferred f_{NL} .

To test this, we allow more flexibility in the FoG model, letting it evolve in redshift in the same manner that our bias model evolves (with Chebyshev polynomials, see Eq. (16)). With this new FoG model, we redo the inference, fitting for the bias parameters, f_{NL} , and the FoG parameters, for two sets of cuts: using $8 < \ell$ and $65 < \ell < 96$ for both the data and one randomly chosen EZmock. In the scenario that the FoG model was previ-

ously insufficiently complex and forced f_{NL} to take on a very negative value, the f_{NL} values of the $65 < \ell < 96$ data sample may see its inferred f_{NL} moved towards zero as the FoG model changes to capture features in the data

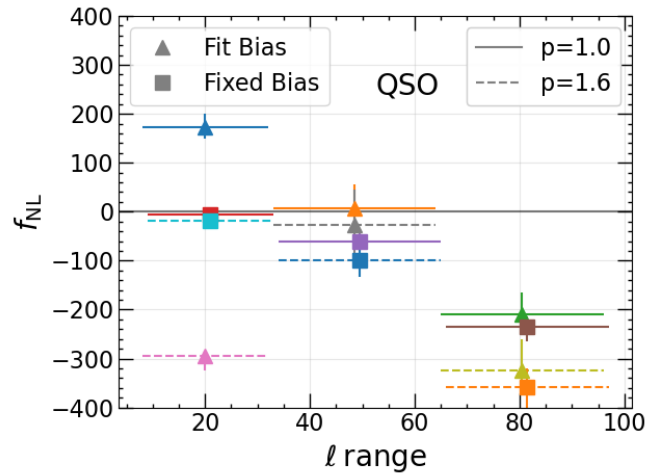


FIG. 10. Similar to Figure 9 but varying fixing versus fitting the bias parameters and only showing QSOs for clarity. When bias parameters are assigned instead of fit, the lowest ℓ bin is consistent with zero, highlighting that the ill behaved bias parameters are responsible for the sporadic f_{NL} behavior as a function of p in Figure 9. Note that the bias must be fit in conjunction with f_{NL} in a proper analysis.

vector that were mimicking a strong negative f_{NL} signal. The EZMocks and $8 < \ell$ samples will serve as some controls to better understand the behavior.

We show in Figures 11 and 12 the corner plots for the $8 < \ell$ and $65 < \ell < 96$ samples, respectively, with the data in blue and the EZmock in orange. For the $8 < \ell$ sample (Figure 11), the f_{NL} and FoG parameters all agree quite well. There is a difference in the fit bias parameters between the EZMock and the data, but this is not relevant to the test we are considering at the moment.

In the $65 < \ell < 96$ samples, Figure 12, we see that the EZmock's f_{NL} is fairly consistent with zero while the data still fits an f_{NL} value of ~ -250 . The FoG parameters between the EZMock and data are somewhat different; the data more strongly favors FoG parameter values away from zero. Note that the FoG parameters enter the model through a squared term (Section IIB1), and so the positive and negative values for a given FoG parameter are equivalent, hence the symmetry across zero. Regardless, we do not see the value f_{NL} change when we opened up the FoG fitting and allowed the model more evolution, so the extremely large negative f_{NL} value is not being driven by inflexible FoG modeling.

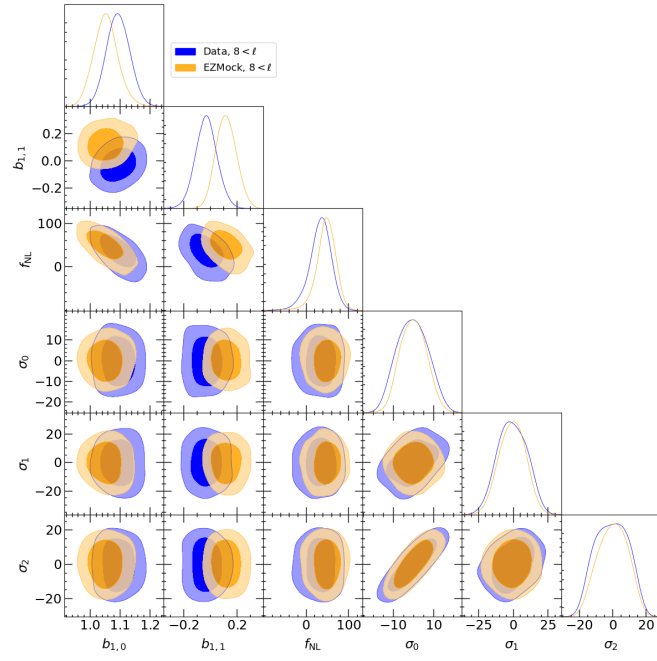


FIG. 11. Corner plots for inferred biases, f_{NL} , and FoG parameters for the QSO sample (blue) and one randomly chosen EZmock (orange) both with $\ell_{\text{min}} = 8$. The most notable features are that 1) the FoG parameters agree well and 2) the bias parameters are in tension.

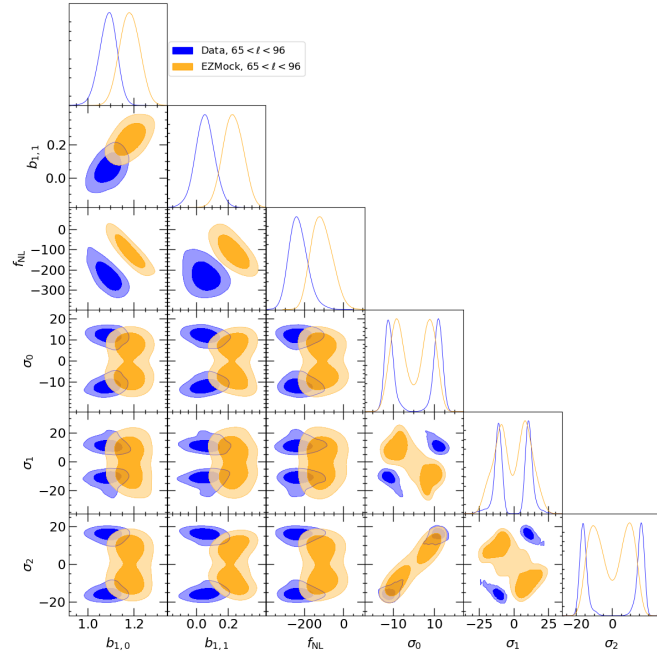


FIG. 12. Similar to Figure 11 except applying the cut $65 < \ell < 96$. Though the data favors FoG parameter values that are farther from zero than the EZMock, the f_{NL} value still peaks at ~ -250 , indicating that an insufficiently flexible FoG model was not attributable for the extremely negative f_{NL} values in Figure 7.